Effect of composition on the structure and electrochemical properties of lithium- and manganese-rich transition metal oxides

Alpesh Khushalchand Shukla[a,b], Quentin M. Ramasse[a], Colin Ophus[c], Despoina Maria Kepaptsoglou[a], Fredrik S. Hage[a], Christoph Gammer[d], Charles Bowling[e], Pedro Alejandro Hernández Gallegos[e], Subramanian Venkatachalam[e]

[a]*SuperSTEM, Daresbury, UK*
[b]*Energy Storage and Distributed Resources Division, Lawrence Berkeley National Laboratory, Berkeley, California, USA*
[c]*National Center for Electron Microscopy, Molecular Foundry, Lawrence Berkeley National Laboratory, Berkeley, California, USA*
[d]*Erich Schmid Institute of Materials Science, Leoben, Austria*
[e]*Envia Systems, Newark, California, USA*

Abstract

Altering the composition of lithium- and manganese-rich transition metal oxides used in lithium ion batteries may have a dramatic impact on their long-term viability as storage solutions for clean-energy automotive applications. Their structure has been widely debated: conflicting conclusions drawn from individual studies often considering different compositions have made it challenging to reach a consensus and inform future research. Here, complementary electron microscopy techniques over a wide range of lengthscales reveal the effect of lithium-to-transition-metal-ratio on the surface and bulk structure of these materials. We found that decreasing the lithium-to-transition metal-ratio resulted in a significant change in terms of order and atomic-level local composition in the bulk of these cathode materials. However, throughout the composition range studied, the materials were made up of just the monoclinic phase, with some chemical ordering defects that increased with a decrease in lithium content. In contrast, the spinel-structured surface present on specific crystallographic facets exhibited no noticeable structural change with composition. This observation warrants a re-examination of phase transformation studies, which have assumed that the surface structure of the pristine materials is the same as in the bulk.

Advances in the electrification of vehicles and the successful implementation of a decentralized electricity grid that efficiently utilizes renewable energy sources is largely dependent on the development of materials that would result into energy storage systems with substantially superior energy density, cycle life and safety compared to those provided by the state-of-the-art batteries. Applications such as electric cars specifically require batteries that exhibit not only very a high capacity to alleviate range anxiety, but also longer lifetimes and demand higher standards of safety. It is known that increasing the lithium content in layered transition metal oxides materials ($LiMO_2$, where M refers to a combination of transition metals such as cobalt, manganese and nickel) to a general composition of $Li_{1+x}M_{1-x}O_2$ can lead to much higher capacities, typically more than 250 mAh/g [1]. However, in spite of the increased capacities found in Li- and Mn-rich transition metal oxides (referred to as LMRTMO in general, where x > 0 and LMR NMC where the transition metals are specifically nickel, manganese and cobalt), their commercial application has been hindered by severe shortcomings in the materials, including a large first-cycle irreversible capacity loss [2], voltage and capacity fade [3], DC resistance rise at low state of charge and transition metal dissolution [4]. Most of the LMRTMO compounds studied so far have a relatively high lithium-to-transition metal (TM) ratio of around 1.5. Recent electron microscopy studies on these materials have shown that their bulk structure consists of domains corresponding to monoclinic variants [5, 6], while the surfaces of certain facets consist of a spinel structure [6]. It could be argued that decreasing the amount of extra lithium could mitigate the aforementioned issues, albeit at the cost of reduced capacities considering the fact that these issues are less severe in layered oxides without excess lithium. However, there have been very few studies on LMRTMOs with intermediate Li/M ratios. Furthermore, to our knowledge the only study on effect of composition on structure was performed on LMRTMO with manganese and nickel [7, 8], and no detailed study on LMR NMC, a more popular cathode material owing to its higher capacity, has been reported thus far. The majority of available literature deals with either "stoichiometric" $LiMO_2$ or Li-rich chemistries with high Li/TM ratios such as $Li_{1.2}M_{0.8}O_2$, where M is typically Mn, Co and Ni or LMRTMOs with a much higher Li/TM ratio. The structure of these materials with lower Li/TM ratio and its effect on electrochemical properties are not clearly understood.

In this paper, we analyze several LMR NMC compositions with varying Li/TM ratio and systematically study the effect of bulk and surface structure on the electrochemical performance of these cathode materials. From an applications point of view, the study was conducted with a goal to find an optimum composition that could maximize the cathode material's energy while reducing the voltage fade over cycling. Samples with three different Li/M ratios were studied using electron

microscopy techniques such as high angle annular dark field (HAADF) imaging in the scanning electron transmission microscope (STEM), electron energy loss spectroscopy (EELS), X-ray energy dispersive spectroscopy (XEDS) and virtual images formed from STEM diffraction images recorded at many probe positions.

Electrochemical measurements

Figure 1a shows the high specific capacities and cycling stability exhibited at high voltage when increasing lithium and manganese contents in the cathode. Figures 1b and 1c, however, illustrate that this high capacity is achieved at the cost of increased voltage fade over many cycles and more low voltage activity is present on discharge, likely associated with a phase transformation in the cathode material. This low voltage electrochemical activity directly correlates with an increase in DC-resistance at lower states of charge, as seen in Figure 1d. It is desirable to keep this resistance low across the entire operating voltage range, to access a higher power density and more overall utilization of the cell's energy. Understanding this material behavior from a structural perspective is central to explaining the electrochemical response, and can lead to future solutions addressing growth in cell resistance.

X-ray diffraction

In order to study the effect of composition on the structure of LMR NMC materials, three materials with different Li/TM ratios were prepared. The compositions of these three materials are shown in Table 1. Figure 2 shows the X-ray diffraction patterns of these three materials. As shown in Figure 2b, the intensity of peaks found between 20° to 30° decreases with a decrease in Li/TM content. At the lowest value of Li/TM, the XRD pattern has a closer resemblence to that of layered oxides with a trigonal structure. However additional peaks between 20° and 30° are still visible. It has been argued that XRD patterns cannot be used to confirm if the LMR NMC materials are two-phased, consisting of trigonal and monoclinic components, or single-monoclinic-phased [9]. Moreover, small peaks in this range of angles can also arise from a $P3_112$ structure that consists of ($\sqrt{3}$ X $\sqrt{3}$) R30° superlattice ordering of the Mn, Ni and Co in the transition metal layer [10]. Therefore, a closer examination using techniques that provide higher spatial resolution, such as aberration-corrected STEM, was warranted. In the following sections, results from various electron microscopy experiments on these three compositions will be presented.

Structure of LMR NMC with high Li/TM ratio

The structure of LMR NMC with a Li/TM ratio of 1.35 is shown in Figure 3. The structure is similar to that observed in a recently published study on LMR NMC with high Li/TM ratio [6] and also to other LMRTMOs such as $Li_{1.2}Ni_{0.2}Mn_{0.6}O_2$

[5]. Only a brief description is therefore provided here. Figure 3b shows a typical HAADF image taken in $[100]_{supercell}$ direction, where the subscript supercell refers to a cell made by randomly stacking three variants of monoclinic structure fitted in an orthorhombic unit cell as described in reference [6]. The HAADF image exhibits the presence of doublets that correspond to transition metal columns, separated by a column with lower intensity that consists of both transition metals and lithium (called the "shared column" henceforth). The HAADF image also demonstrates the presence of domains that correspond to three different variants of monoclinic structure, namely, [1 0 0], [1 $\overline{1}$ 0] and [1 1 0], shown using orange, blue and green colors, respectively. These variants give rise to streaks in a diffractogram as the individual reflections from these variants are very close to each other, as shown in the inset of Figure 3a. The intensity of the shared column is relatively consistent throughout the primary particle except for the variation due to the change in thickness, since the image was taken from a tapered region near the edge of the particle, as shown in Figure 3a. Any non-uniformity in this pattern is only occasional, but has slightly higher occurrence than that observed in LMR NMC with higher lithium, such as $Li_{1.2}Ni_{0.13}Mn_{0.54}Co_{0.13}$ [6]. EELS and XEDS maps taken with sub-nanometer resolution over several areas in different particles exhibited relatively uniform distribution of transition metals except at certain facets, where higher concentration of nickel was observed as shown in Figure 4.

Structure of LMR NMC with medium Li/TM ratio

As shown in the HAADF STEM image in Figure 5b that was taken using the $[100]_{supercell}$ zone axis, the amount of transition metal in the shared column increases as compared to the high Li/TM sample and therefore the doublets, although present, are not as clearly seen. This effect can be observed more clearly in the line profiles shown in Figure 5c. In contrast to the high Li/TM sample, the ratio of Li to TM in this shared column appears random in some of the rows. It should be noted that the intensity of the columns suggest that there is no mixing of Li and TM in the columns corresponding to the doublets and they most likely consist of transition metals only. The Fourier transform (FFT) of the image (shown in inset of Figure 5a) shows the two streaks between the rows of fundamental spots, which are characteristic of the structure consisting of three monoclinic domains. The domains corresponding to [1 0 0], [1 $\overline{1}$ 0] and [1 1 0] can still be identified, although not as clearly as in the case of the high Li/TM sample. This structure was observed throughout the primary particle. It can be thus said that the entire structure consists of (disordered) monoclinic phase, which additionally exhibits local compositional variations. The Li/TM ratio of the shared columns is not constant throughout the particle, which results in some disorder in the structure. Similar to the high Li/TM ratio sample, EELS maps taken with sub-nanometer resolution over several areas in different particles showed a relatively uniform distribution of transition metals, except for certain facets as shown

in Figure 6.

Structure of LMR NMC with low Li/TM ratio

The sample with the smallest Li/TM ratio was studied in detail using HAADF imaging performed at various zone axes, giving a complete, 3-dimensional characterisation of its structure. As shown in Figure 7a, the randomness of Li/TM ratio in the shared column described in the previous section is further increased in HAADF images taken using $[100]_{supercell}$ zone axis. This is shown more clearly in the image with higher magnification (Figure 7b) and the line profiles shown in Figure 7c that correspond to the rows of atomic columns shown in Figure 7b. Certain rows show doublets like those seen in LMR NMC with a high Li/TM ratio (for example lines 2, 4, 5, 10 and 12), because the Li/TM ratio in the shared column is high. In some rows, a lower Li/TM ratio in the shared column leads to rows that do not show the doublet character clearly as shown in lines 3, 6, 8, and 11. Moreover, in many cases, this pattern changes even within the same row, with a few columns showing higher Li/TM ratio in the shared column (giving a doublet character) followed by several columns with lower Li/TM ratio, as shown in rows 1 and 6. The stacking of rows with higher and lower Li/TM ratio appears to have no ordering at the observed length scales. Thus, there is a lack of long range order and areas with high Li/TM ratio and those with low Li/TM ratio in the shared column are not extended over several nanometers. It should be noted that this apparent difference in structure, showing discontinuous rows of atomic columns with doublets and without is simply due to local compositional variation, while the symmetry is the same for both kinds of regions. Both regions, with or without the appearance of doublets, are monoclinic. Furthermore, although there is a variation of composition at the atomic scale as shown by the HAADF STEM images, the distribution of transition metals in the bulk at the nanometer scale remains uniform, as shown in the EELS maps (Figure 8), except at certain facets that exhibited higher concentrations of nickel.

Recent studies on LMRTMOs have suggested a presence of separate monoclinic and trigonal phases based on observation of elemental segregation, whereby Mn-rich areas are assigned to a monoclinic phase while remaining areas are assigned to a trigonal phase [11, 12]. It should be noted that although we observe a relatively uniform distribution of transition metals in the bulk of samples for all the compositions investigated in this study, observation of any non-uniformity in elemental composition does not necessarily imply the presence of a two-phase composite structure consisting of separate (monoclinic) and (trigonal) phases. Moreover, the homogeneity reported here refers to the results obtained from single grains (excluding any surfaces) and not over secondary particles as described in these reports that either involved grain boundaries between primary particles or Ni-rich surfaces. It has also been shown that even particles that appear to be made up of a single grain can in fact consist of several grains as shown recently by Yu et al [13]. The origin of the presence of these grains within a primary particle can be attributed to the presence of several equivalent {1 1 1} planes in the parent NaCl structure as described in detail by Jarvis et al [14] for $Li_{1+x}MnNiO_2$. The presence of these grains with different orientations and the resulting hidden surfaces within a primary particle further complicates structure determination of LMR NMC. Indeed, high resolution HAADF STEM imaging and spectroscopy results obtained over discrete grains have shown that these elemental segregations are limited to surfaces, in agreement with our results [15]. The presence of grain boundaries within a primary particle is more common in LMRTMO prepared using co-precipitation, a method used more commonly in commercial cathode materials, as compared to those prepared by molten salt method, which mostly results in discrete particles consisting of single grains [6, 16].

HAADF images taken using the $[1\,0\,3]_{monoclinic}$ zone axis, which is orthogonal to the previously-discussed $[100]_{monoclinic}$ direction, further help in understanding the structure of LMR NMC. A HAADF image taken from a single variant of a LMR NMC with high Li/TM ratio would consist of two rows of atomic columns consisting of transition metals separated by a row of atoms with mixed Li and transition metals, giving a striped pattern. Three variants that are rotated 120° from each other would give rise to a criss-cross pattern as described in reference [6]. In the case of NMC with pure trigonal structure without any ordering of the transition metals, the intensity of all the columns (in the equivalent $[0\,0\,1]_{trigonal}$ direction) would be equal. In figure 7d, which shows the HAADF image taken on LMR NMC with low Li/TM ratio using a $[1\,0\,3]_{monoclinic}$ zone axis, a criss-cross pattern is clearly observed, but the column intensities are not uniform across the field of view, displaying a level of randomness at this length-scale. Furthermore, the diffractogram clearly shows extra spots present at 1/3rd and 2/3rd distance from the fundamental spot, confirming the presence of all three monoclinic variants. Imaging the sample along the $[0\,0\,1]_{monoclinic}$ direction, on the other hand, gives a HAADF image that apparently looks very uniform. This apparent absence of disorder in this projection is observed because the variants of monoclinic are stacked in such a way that columns corresponding to a mixture of transition metals and lithium sit directly above a column consisting purely of transition metals, thus giving an averaged intensity for each column that appears uniform throughout the particle, as one would observe in a $[0\,0\,1]$ direction of a pure trigonal phase. Faint {1 1 0} and {1 2 0} reflections can barely be seen in an FFT diffractogram taken from a HAADF image consisting of primarily (or only) one monoclinic variant. However, these reflections can be easily observed using an electron diffraction pattern as shown in Figure S1b, exemplifying how FFTs do not necessarily provide the same information as that obtained from electron diffraction patterns. These results also highlight the importance of using multiple techniques and zone axes for solving complex structures: While electron diffraction is more ambiguous for the $[1\,0\,3]_{monoclinic}$ direction than HAADF imaging, it can be useful for avoiding ambiguity from HAADF imaging for the $[0\,0\,1]_{monoclinic}$ direction.

In order to confirm that the structure of LMR NMC with a low Li/TM ratio consists of only the monoclinic structure throughout the primary particle, we performed STEM diffraction imaging experiments, where a 2D image of the diffracted STEM probe was recorded over a 2D grid of probe positions, forming a four dimensional data that we will hereafter refer to as a "4D-STEM experiment." These 4D-STEM experiments allow diffraction mapping on particles with large fields of view at high spatial resolution [17–19]. Figure 9a shows an electron diffraction pattern that was summed using 5625 individual diffraction patterns obtained using a probe size of approximately 2 nm and a step size of 2 nm. The pair of streaks between the rows of the brighter fundamental reflections are observed due to the closeness of diffraction spots corresponding to the [1 0 0], [1 $\bar{1}$ 0] and [1 1 0] variants of the monoclinic phase as described in Figure S2 in Supplementary Information. Figure 9b shows the virtual apertures used for these three variants. The fundamental reflections, shown in gray are common for all three variants. As shown in Figures 9c, d and e, the individual variants are not resolved as rows of atoms except for thin areas in the edges due to the aforementioned randomness in this structure, unlike the case of LMR NMC with a high Li/TM ratio shown in a previously published study [19] where the variants are clearly resolved using this technique. However, it can be noticed that the intensity from these three monoclinic variants are present roughly equally throughout the crystal. None of the 5625 frames in the dataset exhibited diffraction patterns without the streaks. The experiment was repeated using a step size of 5 nm over the entire primary particle, and identical results were obtained as shown in Figure S3 in the supplementary section. These observations show that there are no areas having long range order with a trigonal structure throughout the crystal (which would give only fundamental reflections without the streaks).

It can be argued, however, that each diffraction pattern in the 4D-STEM data is an averaged diffraction pattern taken through the thickness of the sample, and the presence of any pure trigonal regions in the direction of the electron beam will not be observed in these patterns. To confirm that the entire particles indeed consisted of only the monoclinic phase throughout the particle and there was no misinterpretation due to the projection problem, we performed 4D-STEM experiments on the same particle using several zone axes and found identical results. Figures S4 in Supplementary Information shows the results obtained using the [3 0 2]$_{monoclinic}$ zone axis. Electron diffraction simulations for the monoclinic phase with a single variant in the [3 0 2] direction and a supercell made using three monoclinic variants are shown in Figure S5 (Supplementary Information), along with an electron diffraction pattern for a trigonal structure in its equivalent direction ([7 $\bar{7}$ 2]). Although the slabs of monoclinic domains would overlap each other in this orientation, the spots corresponding to the monoclinic variants are well-separated and the 4D STEM diffraction maps show that the entire particle is made up of a single, monoclinic phase.

Although it is clear from these results that over the LMR NMC is not a "composite" material consisting of "structurally integrated" domains of Li_2MnO_3 and $LiNiMnCoO_2$ as suggested by earlier reports [1, 3, 20, 21], there is another structural model that also warrants consideration. Extra reflections in electron diffraction patterns in layered oxides, both with stoichiometric (Li = 1) and lithium-excess compositions have been attributed to long range ordering of the type ($\sqrt{3}$ x $\sqrt{3}$) R30°[10, 22, 23]. Meng et al. [22] proposed that in the case of $LiNi_{0.5}Mn_{0.5}O_2$ and $Li_{1.11}Ni_{0.3}Mn_{0.55}O_2$, there is an in-plane ($\sqrt{3}$ x $\sqrt{3}$) R30°ordering of Li, Mn and Ni ions such that the overall symmetry of the crystal is P3$_1$12 with some C2/m stacking. Yabuuchi et al. [10] and Weill et al. [23] proposed similar in-plane ordering based on electron diffraction studies for materials containing Ni, Mn and Co. We also considered this possibility for the presence of faint reflections and streaks in electron diffraction patterns, although they can be clearly attributed to the presence of the three monoclinic variants. We found that although the electron diffraction patterns simulated using a unit cell with a superstructure matches the experimental diffraction patterns for certain zone axes (such as [0 0 1]$_{trigonal}$), the model fails for other zone axes, even high symmetry ones such as [0 1 0] and [$\bar{1}$ 1 0] as shown in Figure S6 in Supplementary Section, which shows electron diffraction patterns simulated using the unit cell described in Reference [10]. In fact, in a later publication, Boulineau et al. [24] described using a model example of monoclinic Li_2MnO_3 how a superstructure was not needed for the interpretation of these extra reflections and how they can be described simply by the stacking of variants of the monoclinic phase, as we suggest here. We agree with this interpretation and our results show that this is true for LMR NMC over a wide range of compositions. This does not suggest that there is no short range ordering or clustering, but the simulations make it clear that the extra reflections and streaks in electron diffraction patterns are formed principally due to the presence of monoclinic variants rather than to long range ($\sqrt{3}$ x $\sqrt{3}$) R30° ordering of transition metals. The latter would also lead to extra reflections in the row of fundamental reflections, as shown in Figure S5 in Supplementary Information, which is clearly not observed in experimental patterns as shown in Figure S1.

McCalla et al. studied the effect of cooling rate on combinatorial samples prepared for a Li-Co-Mn oxide system [25]. Although their system did not contain Ni, some of their findings can be related to the results obtained in the present study. They found that phase separation occurs for layered oxides synthesized using a very slow rate of cooling (∼ 1 °C/min), while it does not occur for samples prepared using intermediate cooling rates (∼ 10 °C/min), as used in the case of our samples and most commercial cathode materials. It was noted that at intermediate cooling rates, the system does not have sufficient time to make larger crystallites for each phase. They also observed that XRD patterns for the samples with compositions between $LiCoO_2$ and Li_2MnO_3 that showed phase separation exhibited peak splitting, especially at the peaks around 45° and 65° 2θ, a feature that was absent in our XRD patterns. It should be noted that the phase separation for the compositions discussed by McCalla et al. do not refer to a coexistence of $LiCO_2$ and

Li$_2$MnO$_3$ phases.

Effect of composition on surface structure

Several studies have shown that the surface of LMR NMC has a different structure and composition than the bulk [26, 27]. In a recently-published study on LMR NMC with higher Li/TM ratio [6], it was demonstrated that this surface is a spinel (typically Ni and/or Co enriched, based on the composition) and has an orientation relationship with the bulk given by $(0\,0\,1)_M \parallel (1\,\bar{1}\,1)_S$, $[0\,1\,0]_M \parallel [1\,1\,0]_S$, where subscripts M and S refer to the monoclinic and spinel phases, respectively. The role of this spinel surface layer vis-à-vis that of the bulk on electrochemical cycling and problems such as voltage fade and DC resistance rise is not clearly understood, in spite of several studies that have discussed the role of phase transformations on the surface of the cathode particles [28–31]. In order to investigate the influence, if any, of Li/TM ratio on this surface layer and ultimately on the electrochemical performance of the cathode material, we studied the surface of the LMR NMC with the aforementioned compositions using HAADF STEM imaging, 4D-STEM, EELS and XEDS. We found that the Li/TM ratio hardly had any effect on the thickness, structure or composition of this surface layer. All the LMR NMC samples, irrespective of the composition, exhibited a spinel layer. EELS and XEDS experiments suggested that all the spinel surfaces exhibited a higher concentration of nickel at the expense of a lowering of manganese content at the surface as shown in Figures 4, 6 and 8. Figure 10 shows this spinel layer at higher resolution. Figures 10a and b show HAADF images taken on LMR NMC with medium Li/TM ratio using the $[1\,0\,3]_{\text{monoclinic}}$ zone axis, where an approximately 2 nm thick spinel surface layer having a $[1\,1\,2]$ zone axis is clearly visible. Similarly Figures 10 c and d show $[1\,1\,0]_{\text{spinel}}$ surface on LMR NMC with the lowest Li/TM ratio in $[0\,\bar{1}\,0]$ zone axis.

As discussed earlier, non uniformity of transition metal distribution reported in recent reports on samples with multiple grains can be attributed to the presence of grain boundaries and surfaces that are richer in Ni and Co . Figure 10d demonstrates how these non-uniformities can be observed even in case of a single grain. It is well-known that crystals often contain growth ledges [32], such as one shown using a red arrow in Figure 10d, which shows a hidden surface layer containing the spinel structure. Since the spinel surface is rich in nickel, an XEDS map taken in projection would show an area with relatively higher manganese content sandwiched between areas with relatively higher nickel content.

For comparison, we also studied the surface of a "stoichiometric" NMC with a nominal composition of LiNi$_{1/3}$Mn$_{1/3}$Co$_{1/3}$O$_2$ and found that the sample also exhibited a spinel surface with the same orientation relationship with the bulk as observed in LMR NMC studied. The fact that the thickness, relative composition and orientation relationship with the bulk does not change with change in Li/TM ratio suggests that the formation of this spinel layer is common for a wide variety of layered oxides. The materials in this study were prepared using a co-precipitation method described in the methods section, but similar results have been shown in LMR NMC made with other synthesis techniques such as the molten salt method [6, 16]. These studies suggest that the spinel, which most likely forms during the synthesis process, is a common occurrence in a wide range of layered oxides, including both lithium-rich and stoichiometric compositions. The spinel forms only on the unstable facet (which is also the facet corresponding to the path of lithium diffusion) and a few unit cells of spinel acts as a stabilizing layer. The surface of this spinel layer has a {1 1 1} facet, which is known to be a very stable surface [33]. It is not clear if this spinel layer facilitates the diffusion of lithium or hinders it, but the fact that pristine samples did not exhibit any change in the spinel with change in composition suggests that the changes in electrochemical performance (reduced voltage fade, capacity fade and DC resistance rise and decrease in capacity) is most likely due to the changes in the bulk structure of LMR NMC rather than to effects related to this surface layer.

Conclusion

In summary, the present study unambiguously demonstrates for the first time that even a small amount of excess lithium in LMR NMC results in a single phase monoclinic structure rather than in the parent trigonal structure of LiMO$_2$, which is often assumed for layered oxides. While decreasing the lithium content resulted in a significant change in terms of order and atomic-level local composition in the bulk of LMR NMC primary particles, no noticeable change in structure, thickness or composition was observed on the surface spinel layer consistently observed on specific facets of these materials. In the bulk, although the structure across the different compositions consists of an aperiodic arrangement of monoclinic variants, there is an obvious decrease in order as we decrease the Li/TM ratio. The transition metal layer in LMR NMC, when examined along the $[1\,0\,0]$ direction, consists of pairs of columns of transition metals separated by a mixed-content column consisting of both Li and transition metals. The ratio of Li/TM in this column is more or less uniform in LMR NMC with more excess lithium and it becomes random at lower amounts of excess lithium. We did not find regions with pure trigonal (LiMO$_2$) or pure monoclinic phase consisting of manganese only as the transition metal (Li$_2$MnO$_3$). This observation is particularly relevant in the context of a drive towards higher-performance battery cathodes because it is a common practice to use extra lithium during the synthesis of stoichiometric lithium transition metal oxides in order to compensate for the loss of lithium during synthesis, and it is difficult to accurately confirm a stoichiometric composition (Li = 1) in these materials even with well-established techniques such as inductively-coupled plasma mass spectrometry.

These structural observations are all the more important that we have also demonstrated in the case of compositions with lower Li/TM ratio a significant improvement in electrochemical performance, especially with respect to voltage fade

2

and DC resistance rise, albeit at the cost of some decrease in capacity. The fact that the characteristics of the surface do not significantly change with changes in composition suggests that the transformation in the bulk of the cathode material might play a larger role in the manifestation of issues such as capacity fade, voltage fade and DC resistance rise. While there have been very detailed and systematic studies on the effect of cycling on phase transformation at the surface of layered oxides [28, 29], it is often assumed in these studies that the surface has the same crystal structure as that of the bulk. The demonstration of the presence of a surface spinel layer on layered oxides with a wide range of compositions in this study therefore warrants a closer and detailed examination of pristine samples before studying any phase transformation that may occur upon cycling.

Methods

Materials synthesis: The lithium-rich NMC materials were synthesized by co-precipitation reaction, which has been described previously [34]. Typically, stoichiometric amounts of metal sulfates were slowly dripped into a continuously-stirred tank reactor (CSTR), wherein sodium carbonate and ammonium hydroxide were also added. The reaction pH, agitation speed, and the temperature were carefully controlled so as to enable a complete precipitation reaction with a well-defined morphology. The metal carbonate precursor was then mixed appropriately with lithium and calcined to form lithium-rich NMC cathode powders.

Electrode preparation and electrochemical measurements: For coin cell testing, composite electrodes were prepared with 80% by weight of active material, 10% by weight of polyvinylidene fluoride binder (Kureha, Japan), 5% by weight of Super P carbon black (Timcal, Belgium), and 5% by weight of KS6 graphite (Timcal, Belgium) with 1-methyl-2-pyrrolidinone (Sigma Aldrich, USA) as the solvent. The slurry was coated onto aluminum foil then dried in a vacuum at 120 °C for 2 hours. Celgard 2320 separator and a 1.2 M $LiPF_6$ electrolyte solution in ethylene carbonate/dimethyl carbonate (BASF, USA) were used in the coin cells with lithium metal as the negative electrode. The coin cells were tested at different discharge currents corresponding to two cycles each at C/10, C/5, C/3, 1C, and 2C, and then cycled at a C/3 rate for 50 cycles. The half cells were charged to 4.6 V in the first C/10 cycle, then subsequently cycled between 2.0 V and 4.5 V vs. Li/Li+ for all remaining cycles.

For pouch cell testing, composite electrodes were prepared with 92% by weight of active material, along with polyvinylidene fluoride binder and conductive carbon additives, with 1-methyl-2-pyrrolidinone as the solvent. Positive electrodes with an area of 12.75 cm^2, a loading of 15 mg/cm^2, and a density of 2.65 g/cm^3 were punched out of the resulting laminates. The positive electrodes were paired against graphite-based negative electrodes resulting in a ratio of negative to positive total capacity of 108%. The pouch cells were assembled inside an argon-filled glovebox with Celgard 2320 separators and a 1.5 M $LiPF_6$ electrolyte solution in 1:2 v/v ethylene carbonate/dimethyl carbonate. The electrochemical test for the pouch cells consisted of charging the cell at C/20 up to 4.2 V, then relaxing the system for a substantial amount of time so as to stabilize the solid-electrolyte-interface (SEI) formed. After the rest period, the cells were charged to 4.6 V to activate the cathode and discharged to 2.0 V, then cycled a couple of times in the voltage range 2.0-4.4 V before the DC-R measurement was performed.

The DC-Resistance (DC-R) measurement was performed during discharge at every 10% SOC after charging the cell to 4.4 V at a C/3 rate. The cell was discharged at a C/3 rate until 10% of the positive electrode's total specific capacity was extracted; namely, the cell was discharged to 90% state of charge (SOC). After a 1 hour rest, a 1C discharge pulse was performed for 10 seconds, and after a 5 minute rest, a 1C charge pulse was performed for 10 seconds. Subsequently, the cell was discharged until an additional 10% of the positive electrode's total capacity was extracted and the 1C discharge/charge pulses were performed. Altogether, pulsing was performed every 10% SOC between 90-30% SOC and every 2.5% SOC between 30-10% SOC. The resulting area-specific impedance (ASI) in units of Ωcm^2 was computed by multiplying the positive electrode's area by the difference between the cell's voltages after the 1 hour rest and after the 10 second discharge pulse divided by the pulse's applied current (1C).

Electron microscopy All the samples were studied using either a probe-corrected microscope operating at 100 kV accelerating voltage using a convergence angle of approximately 30 mrad and a collection angle for HAADF images that was calibrated at 82-190 mrad (SuperSTEM 2) or a probe-corrected microscope operating at 80 kV accelerating voltage using a convergence angle of approximately 30 mrad and a collection angle for HAADF images of 60-180 mrad (TEAM 0.5). XEDS maps with sub-nanometer resolution were obtained at 120 kV accelerating voltage using an FEI Titan microscope equipped with a quad-detector system. 4D-STEM maps (electron diffraction maps) with resolution ranging from 2 to 5 nm were obtained at 120 kV accelerating voltage using a Digital Micrograph script as described in reference [18]. Samples for electron microscopy were prepared by drop casting a sonicated solution of LMRTMOs and anhydrous ethanol. HAADF STEM simulations were performed using a custom code that was prepared using details provided in reference [35].

Other material characterization: Powder X-ray diffraction (XRD) was carried out with a Rigaku Ultima IV X-Ray Diffractometer using Cu-K-alpha radiation. Elemental analysis was carried out using a Varian 715-ES inductively-coupled plasma optical emission spectrometer (ICP-OES), which determined the molar ratios of Li, Ni, Co, and Mn present in each cathode material. Scanning electron microscopy (SEM) using a Hitachi S4800 was used to assess the quality of samples prepared for the transmission electron microscopy (TEM) grid.

Acknowledgments

also like to thank Mr. Chengyu Song, Dr. Karen Bustillo and Dr. Peter Ercius for their assistance in operating the microscopes at the National Center of Electron Microscopy, Molecular Foundry.

References

[1] Thackeray, M. M., Johnson, C. S., Vaughey, J. T., Li, N. & Hackney, S. A. Advances in manganese-oxide 'composite' electrodes for lithium-ion batteries. *J. Mater. Chem.* **15**, 2257–2267 (2005).

[2] Lu, Z. & Dahn, J. R. Understanding the anomalous capacity of Li/Li [$Ni_x Li_{(1/3 - 2x/3)} Mn_{(2/3 - x/3)}$] O_2 cells using in situ X-ray diffraction and electrochemical studies. *Journal of the Electrochemical Society* **149**, A815–A822 (2002).

[3] Croy, J. R., Kang, S. H., Balasubramanian, M. & Thackeray, M. M. Li_2MnO_3-based composite cathodes for lithium batteries: a novel synthesis approach and new structures. *Electrochem commun* **13**, 1063–1066 (2011).

[4] Kang, S.-H. & Thackeray, M. M. Enhancing the rate capability of high capacity $xLi_2MnO_3 \cdot (1- x)LiMO_2$ (M= Mn, Ni, Co) electrodes by Li–Ni–PO4 treatment. *Electrochem commun* **11**, 748–751 (2009).

[5] Jarvis, K. A., Deng, Z., Allard, L. F., Manthiram, A. & Ferreira, P. J. Atomic Structure of a Lithium-Rich Layered Oxide Material for Lithium-Ion Batteries: Evidence of a Solid Solution. *Chem. Mater.* **23**, 3614–3621 (2011).

[6] Shukla, A. K. *et al.* Unravelling structural ambiguities in lithium- and manganese-rich transition metal oxides. *Nat Comm* **6**, 8711 (2015).

[7] Jarvis, K., Deng, Z. & Manthiram, A. Understanding the role of lithium content on the structure and capacity of lithium-rich layered oxides by aberration-corrected STEM, D-STEM, and EDS. *Microsc Microanal* **18**, 1484–1485 (2012).

[8] Wang, C.-C., Jarvis, K. A., Ferreira, P. J. & Manthiram, A. Effect of synthesis conditions on the first charge and reversible capacities of lithium-rich layered oxide cathodes. *Chem. Mater.* **25**, 3267–3275 (2013).

[9] Mohanty, D. *et al.* Neutron diffraction and magnetic susceptibility studies on a high-voltage $Li_{1.2}Mn_{0.55}Ni_{0.15}Co_{0.10}O_2$ lithium ion battery cathode: insight into the crystal structure. *Chem. Mater.* **25**, 4064–4070 (2013).

[10] Yabuuchi, N., Koyama, Y., Nakayama, N. & Ohzuku, T. Solid-state chemistry and electrochemistry of $LiCo_{1/3}Ni_{1/3}Mn_{1/3}O_2$ for advanced lithium-ion batteries II. Preparation and characterization. *J. Electrochem. Soc.* **52**, A1434–A1440 (2005).

[11] Gu, M., Genc, A., Belharouak, I. & Wang, D. Nanoscale Phase Separation, Cation Ordering, and Surface Chemistry in Pristine $Li_{1.2}Ni_{0.2}Mn_{0.6}O_2$ for Li-Ion Batteries. *Chem. Mater* **25**, 23192326 (2013).

[12] Devaraj, A., Gu, M., Colby, R., Yan, P. & Wang, C. M. Visualizing nanoscale 3D compositional fluctuation of lithium in advanced lithium-ion battery cathodes. *Nat Comm* **6**, 8014 (2015).

[13] Yu, H., So, Y. G., Kuwabara, A., Tochigi, E. & Shibata, N. Crystalline grain interior configuration affects lithium migration kinetics in Li-rich layered oxide. *Nano Lett* **16**, 2907–2915 (2016).

[14] Jarvis, K. A., Wang, C.-C., Manthiram, A. & Ferreira, P. J. The role of composition in the atomic structure, oxygen loss, and capacity of layered Li–Mn–Ni oxide cathodes. *J. Mater. Chem. A* **2**, 1353–1362 (2014).

[15] Yan, P. *et al.* Ni and Co Segregations on Selective Surface Facets and Rational Design of Layered Lithium Transition-Metal Oxide Cathodes. *Adv. Energy Mater.* n/a–n/a (2016).

[16] Kuppan, S., Shukla, A. K., Membreno, D., Nordlund, D. & Chen, G. Revealing Anisotropic Spinel Formation on Pristine Li- and Mn-Rich Layered Oxide Surface and Its Impact on Cathode Performance. *Adv. Energy Mater.* 1602010 (2017).

[17] Ophus, C., Ercius, P., Sarahan, M., Czarnik, C. & Ciston, J. Recording and Using 4D-STEM Datasets in Materials Science. *Microsc Microanal* **20**, 62–63 (2014).

[18] Gammer, C., Özdöl, V. B., Liebscher, C. H. & Minor, A. M. Diffraction contrast imaging using virtual aperturesâĂÍ . *Ultramicroscopy* **155**, 1–10 (2015).

[19] Shukla, A. K., Ophus, C., Gammer, C. & Ramasse, Q. M. Study of Structure of Li-and Mn-rich Transition Metal Oxides Using 4D-STEM. *Microsc Microanal* **22**, 494–495 (2016).

[20] Thackeray, M. M. *et al.* Li_2MnO_3-stabilized LiMO2 (M= Mn, Ni, Co) electrodes for lithium-ion batteries. *J. Mater. Chem.* **17**, 3112–3125 (2007).

[21] Thackeray, M. M., Kang, S. H., Johnson, C. S., Vaughey, J. T. & Hackney, S. A. Comments on the structural complexity of lithium-rich $Li_{1+x}M_{1-x}O_2$ electrodes (M= Mn, Ni, Co) for lithium batteries. *Electrochem commun* **8**, 1531–1538 (2006).

[22] Meng, Y. S. *et al.* Cation Ordering in Layered O3 $Li[Ni_x Li_{1/3−2x/3} Mn_{2/3−x/3}]O_2$ ($0 \le x \le 1/2$) Compounds. *Chem. Mater.* **17**, 2386–2394 (2005).

[23] Weill, F., Tran, N., Croguennec, L. & Delmas, C. Cation ordering in the layered $Li_{1+x}(Ni_{0.425}Mn_{0.425}Co_{0.15})_{1-x}O_2$ materials (x=0 and 0.12). *J Power Sources* **172**, 893–900 (2007).

[24] Boulineau, A., Croguennec, L., Delmas, C. & Weill, F. Reinvestigation of Li_2MnO_3 Structure: Electron Diffraction and High Resolution TEM. *Chem. Mater.* **21**, 4216–4222 (2009).

[25] McCalla, E., Lowartz, C. M., Brown, C. R. & Dahn, J. R. Formation of Layered–Layered Composites in the Li–Co–Mn Oxide Pseudoternary System during Slow Cooling. *Chem. Mater.* **25**, 912–918 (2013).

[26] Dixit, H., Zhou, W., Idrobo, J.-C., Nanda, J. & Cooper, V. R. Facet-Dependent Disorder in Pristine High-Voltage Lithium–Manganese-Rich Cathode Material. *Acs Nano* **8**, 12710–12716 (2014).

[27] Gu, M. *et al.* Conflicting roles of nickel in controlling cathode performance in lithium ion batteries. *Nano Lett* **12**, 5186–5191 (2012).

[28] Lin, F., Markus, I. M., Nordlund, D. & Weng, T. C. Surface reconstruction and chemical evolution of stoichiometric layered cathode materials for lithium-ion batteries. *Nat Comm* **5**, 3529 (2014).

[29] Liu, H. *et al.* Spatially resolved surface valence gradient and structural transformation of lithium transition metal oxides in lithium-ion batteries. *Phys. Chem. Chem. Phys.* **18**, 29064–29075 (2016).

[30] Yan, P. *et al.* Evolution of Lattice Structure and Chemical Composition of the Surface Reconstruction Layer in $Li_{1.2}Ni_{0.2}Mn_{0.6}O_2$ Cathode Material for Lithium Ion Batteries. *Nano Lett* **15**, 514–522 (2014).

[31] Yang, F. *et al.* Nanoscale Morphological and Chemical Changes of High Voltage Lithium–Manganese Rich NMC Composite Cathodes with Cycling. *Nano Lett* **14**, 4334–4341 (2014).

[32] Porter, D. A. & Easterling, K. E. *Phase Transformation in Metals and Alloys* (Chapman & Hall, 1992), 2nd edn.

[33] Karim, A., Fosse, S. & Persson, K. A. Surface structure and equilibrium particle shape of the $LiMn_2O_4$ spinel from first-principles calculations. *Phys. Rev. B* **87**, 075322 (2013).

[34] Lopez, H. A., Venkatachalam, S. & Karthikeyan, D. Layer-layer lithium rich complex metal oxides with high specific capacity and excellent cycling. US Patent Application no. US2014/0234716A1. US Patent Office (2014).

[35] Kirkland, E. J. Advanced Computing in Electron Microscopy. Springer US, Boston, MA (2010).

4

Table 1: Composition of LMRTMOs studied

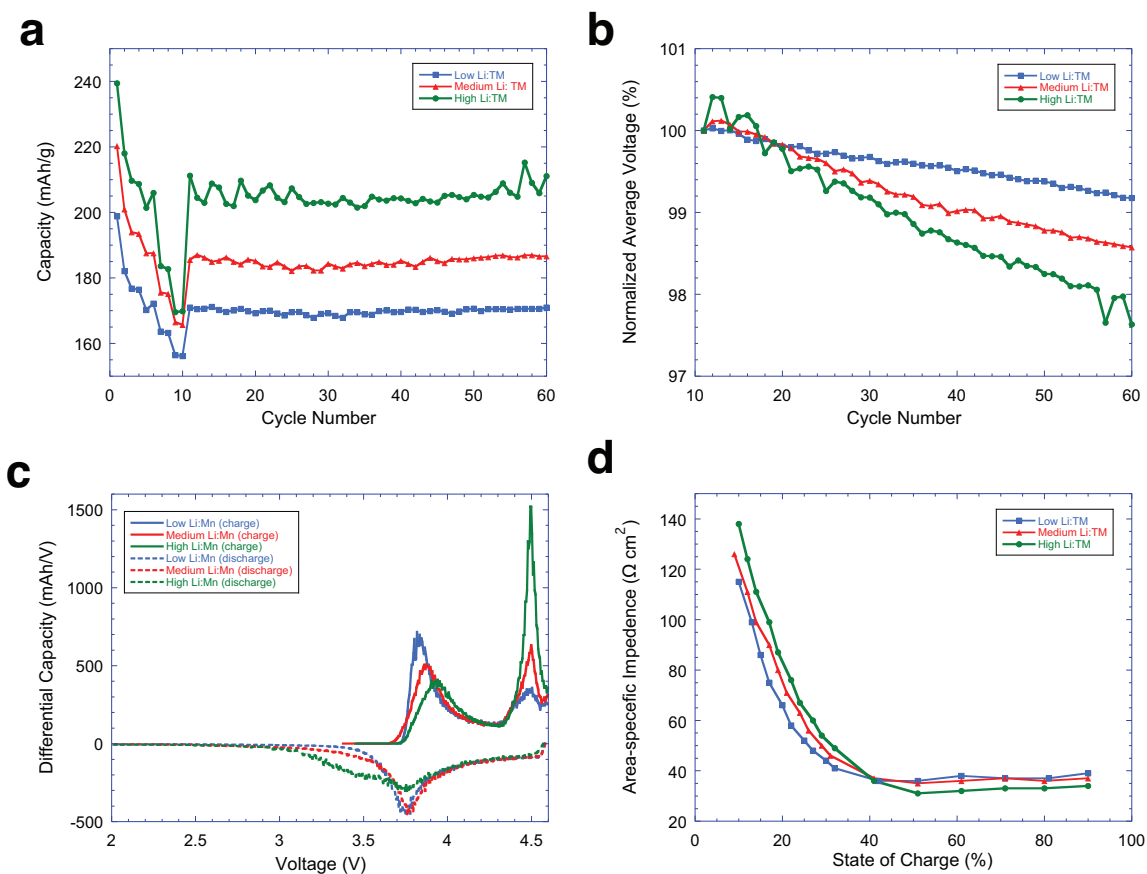| Sample	Li/TM ratio	Chemical formula
High Li:TM	1.353	$Li_{1.15}Ni_{0.1748}Mn_{0.496}Co_{0.18}O_2$
Medium Li:TM	1.222	$Li_{1.1}Ni_{0.227}Mn_{0.438}Co_{0.235}O_2$
Low Li:TM	1.17	$Li_{1.079}Ni_{0.248}Mn_{0.411}Co_{0.263}O_2$

Figure 1: A comparison of electrochemical data for LMR NMC with low, medium, and high Li/M ratios: a) Specific capacity in half cell coin cells over various discharge rates from C/10 up to 2C, then 50 subsequent cycles at a rate of C/3. The first charge was to 4.6 V, then all following cycles were between 2.0-4.5 V vs. Li/Li+., b) Normalized average voltage over the 50 cycles in the half cells, c) Differential capacity plot for the first cycle in the half cells, d) DC-resistance plot for the three systems in pouch cell full cells. The resistance was measured from 1C pulses at every 10% SOC point over a C/3 discharge in the voltage window 2.0-4.4 V.
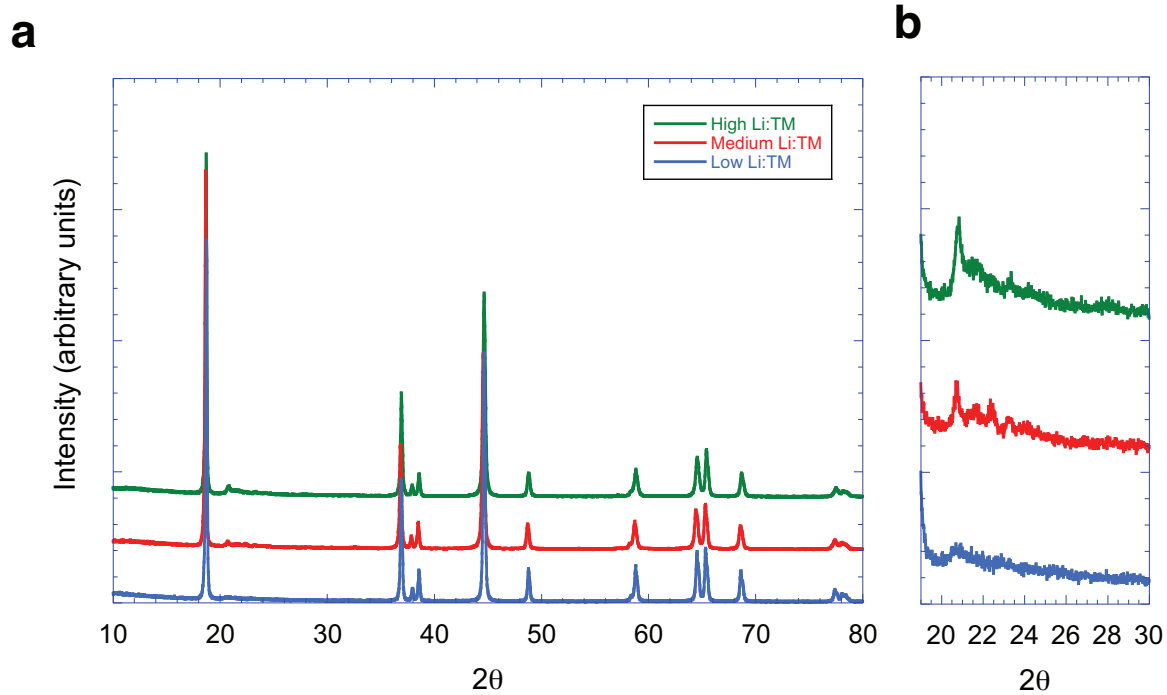
Figure 2: X-ray diffraction: a) X-ray diffraction patterns for LMRTMO with different Li/M ratios, b) X-ray diffraction corresponding to 2θ from 19° to 30° with intensities scaled by a factor of 10 for clarity.
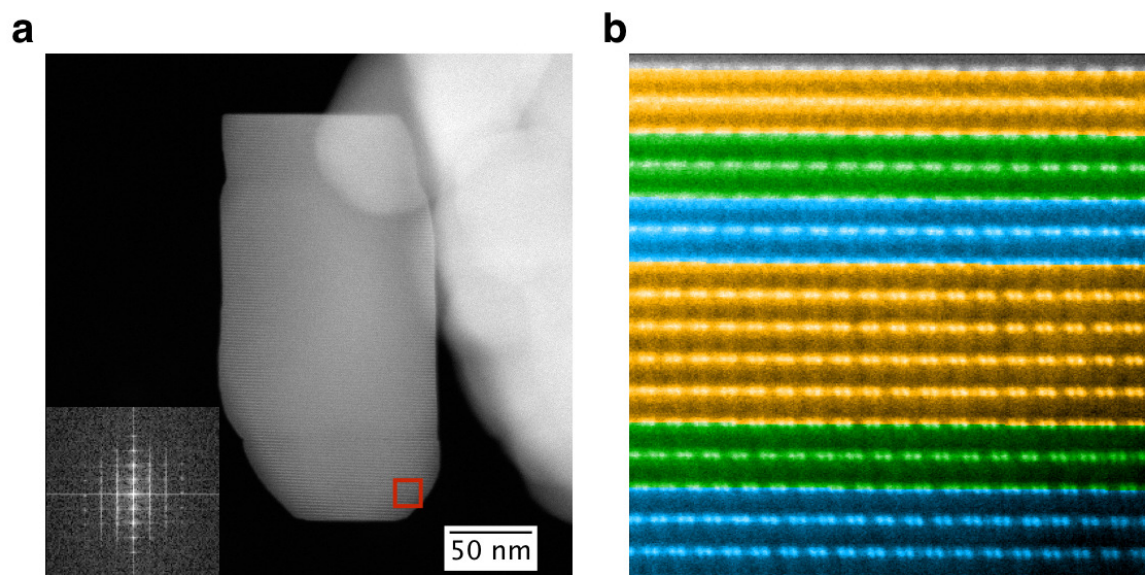
Figure 3: HAADF images for LMR NMC with high Li/M ratio: a) Low magnification HAADF STEM image and b) HAADF STEM image showing domains corresponding to three monoclinic variants. Inset in a shows FFT of b.
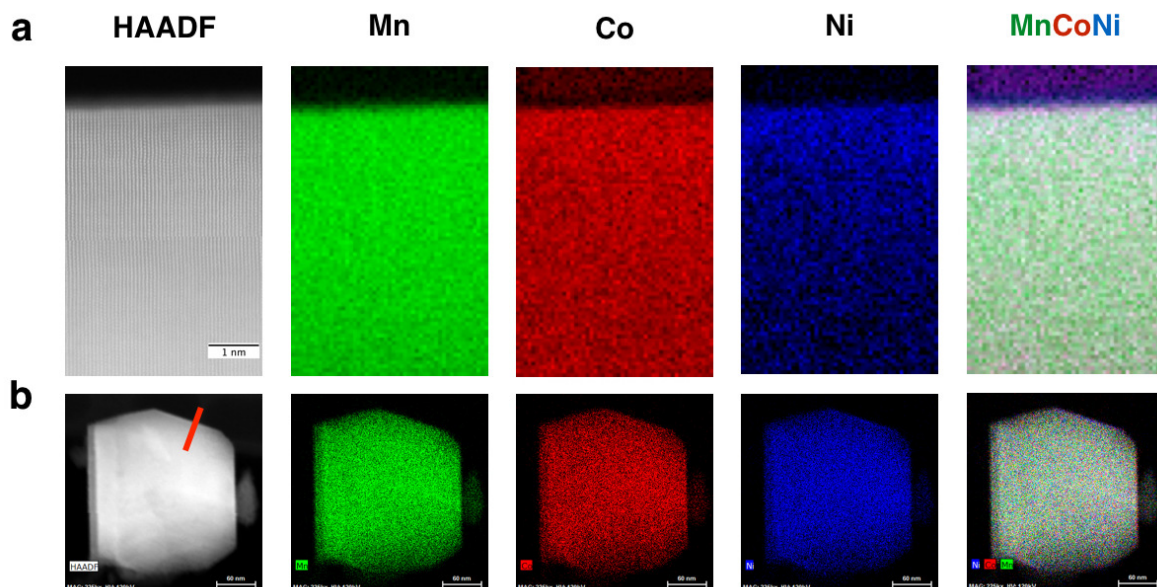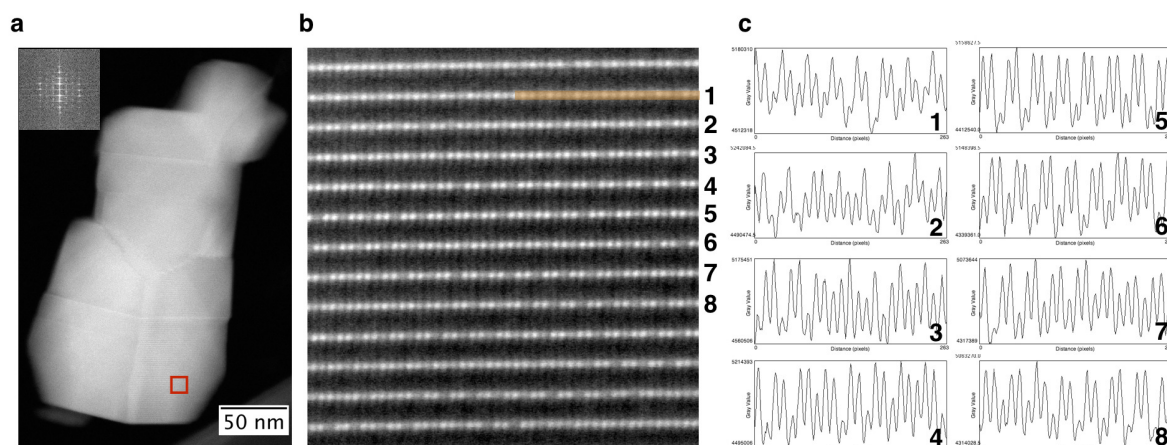
Figure 4: EELS and XEDS maps for LMR NMC with high Li/M ratio: a) EELS map at sub nanometer resolution and b) XEDS map covering an entire primary particle. Both maps show relatively uniform distribution of transition metals except at certain facets, where high concentration of nickel was observed.

Figure 5: HAADF images for LMR NMC with medium Li/M ratio: a) Low magnification HAADF STEM image, b) HAADF STEM image of the area corresponding to the red square in a. Inset in a shows FFT of b, and c) line scans corresponding to eight rows in b. .

8
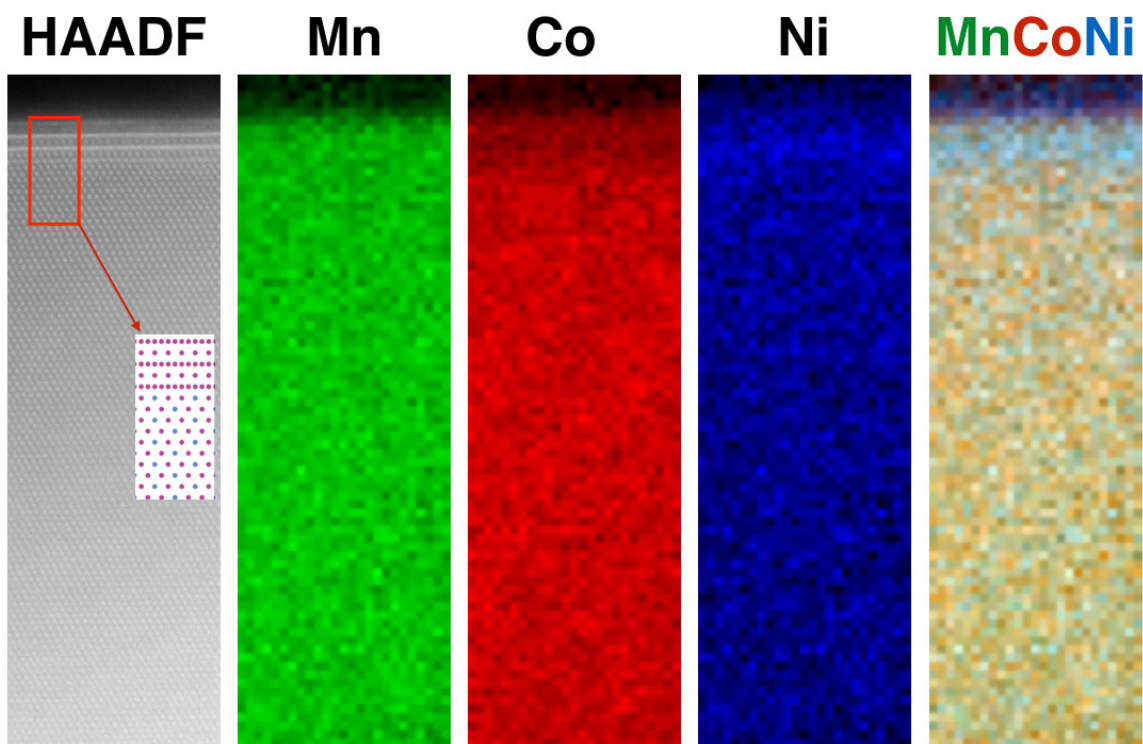
Figure 6: EELS for LMR NMC with medium Li/M ratio: a) HAADF image and EELS maps showing relatively uniform distribution of transition metals except at certain facets, where high concentration of nickel was observed. HAADF image taken at $[0\,0\,1]_{\text{monoclinic}}$ shows surface spinel in $[1\,1\,2]$ zone axis, as previously observed in Reference [6]
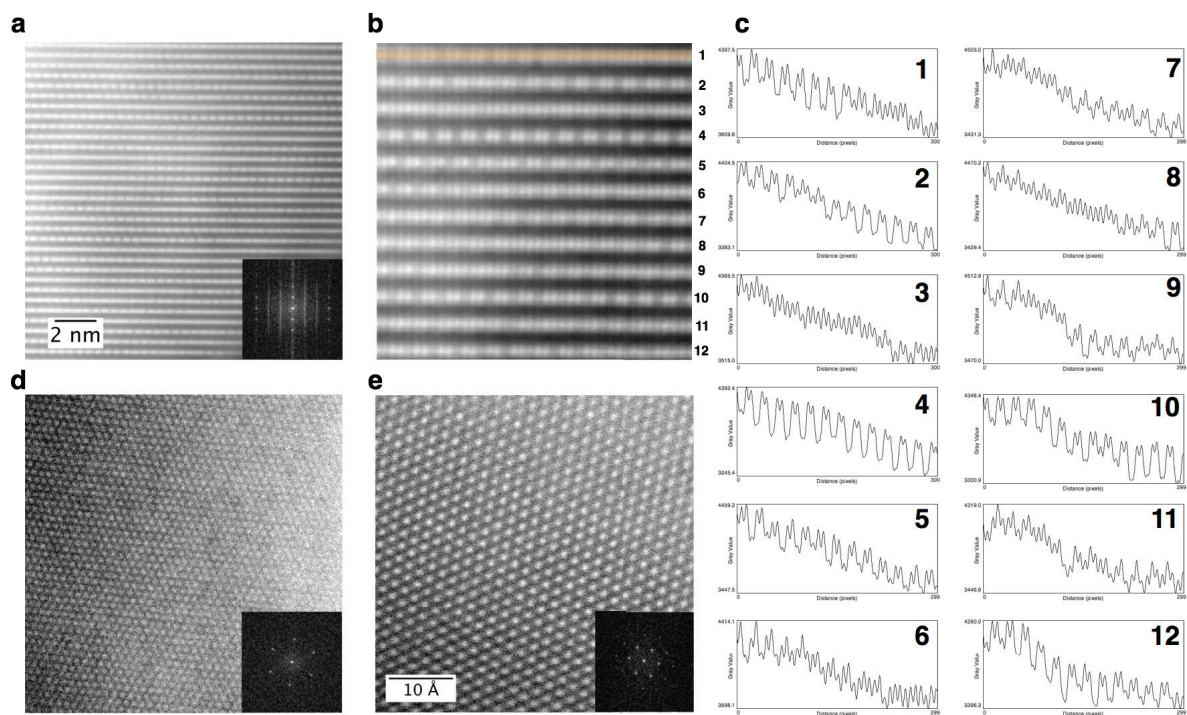
Figure 7: HAADF images for LMR NMC with low Li/M ratio: a) HAADF image taken using $[1\,0\,0]/[1\,\bar{1}\,0]/[1\,1\,0]_{monoclinic}$ zone axis showing loss of order within the domains corresponding to the monoclinic variants, b) HAADF image with higher magnification of a section in a), c) Line scans corresponding to the rows of atomic columns in b), d) HAADF STEM taken using $[1\,0\,3]_{monoclinic}$ zone axis , e) HAADF STEM image taken using $[0\,0\,1]_{monoclinic}$ zone axis.
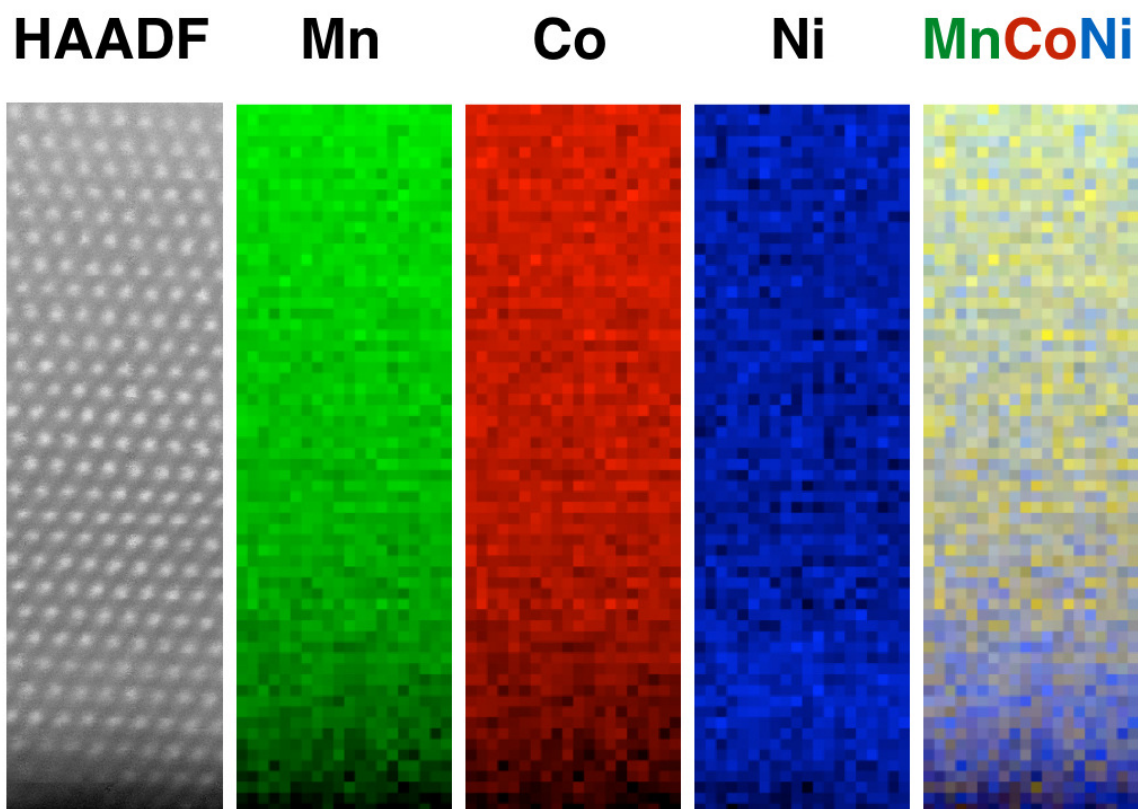
Figure 8: EELS for LMR NMC with low Li/M ratio: a) HAADF image and EELS maps showing relatively uniform distribution of transition metals except at certain facets, where high concentration of nickel was observed. Data was taken using $[0\,0\,1]_{monoclinic}$ zone axis. Spinel surface is not visible on the edge due to the presence of tapered edge.
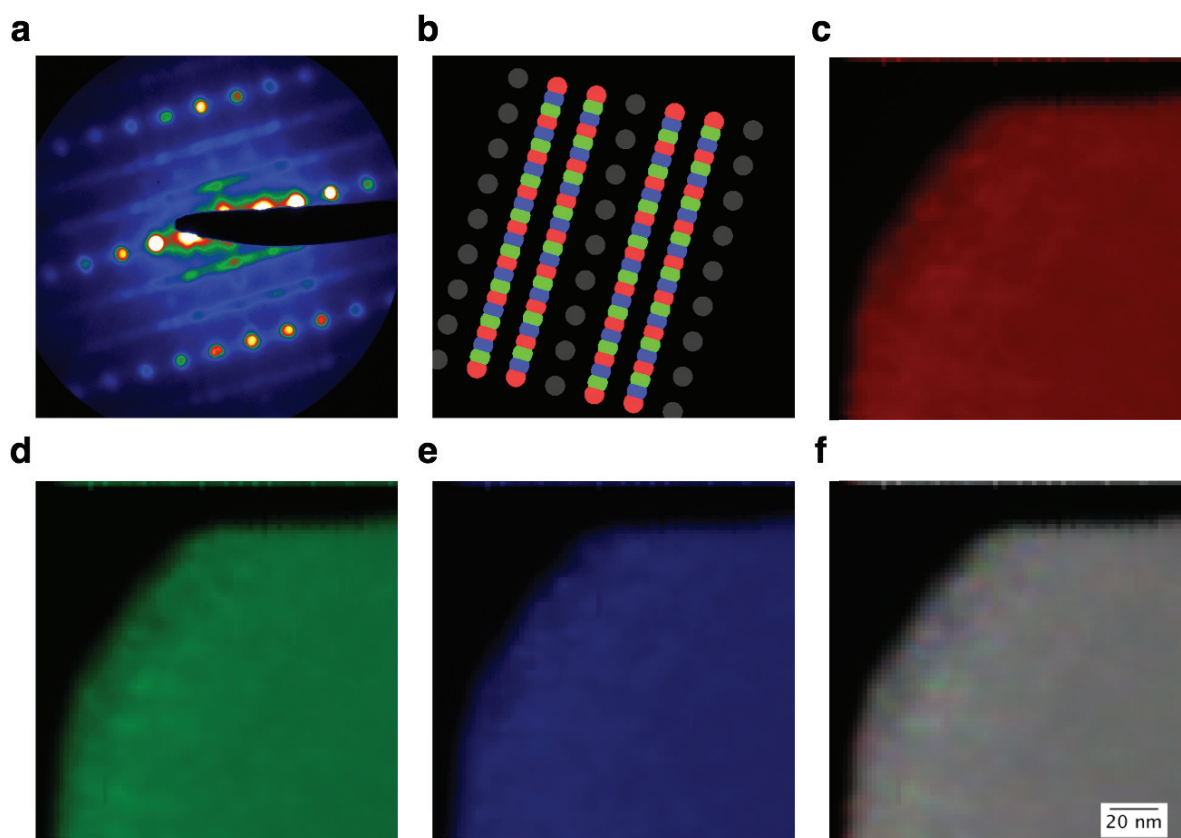
11

Figure 9: 4D-STEM analysis of LMR NMC with low Li/M ratio: a) Summed diffraction pattern taken using $[1\,0\,0]/[1\,\bar{1}\,0]/[1\,1\,0]_{\text{monoclinic}}$ zone axis showing streaks corresponding to the three monoclinic variants b) image showing positions of masks corresponding to the three monoclinic variant, c) virtual dark field image showing variant 1 ($[1\,0\,0]$) d) virtual dark field image showing variant 2 ($[1\,\bar{1}\,0]$), e) virtual dark field image showing variant 3 ($[1\,1\,0]$) and f) virtual dark field image of the LMR NMC particle.

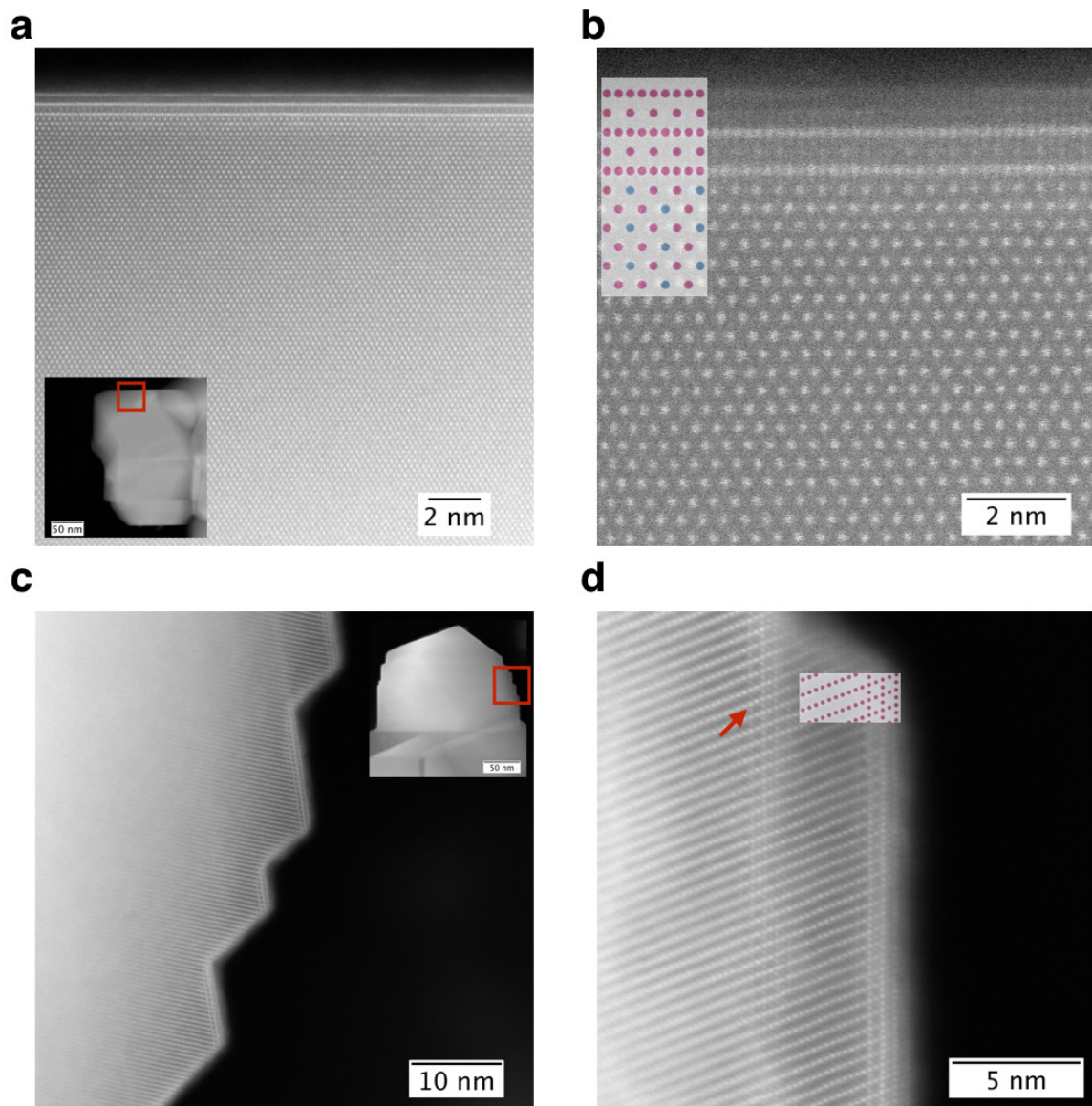Figure 10: HAADF images showing surface spinel on LMR NMC particles: a) and b) HAADF images taken on LMR NMC with medium Li/TM ratio using $[0\,0\,1]_{\text{monoclinic}}$ zone axis, c) and d) HAADF image taken on LMR NMC with low Li/TM ratio using $[0\,1\,0]_{\text{monoclinic}}$ zone axis.

13